The Company of Biologists

RESEARCH ARTICLE

The impact of cell size on morphogen gradient precision

Jan A. Adelmann[1,2], Roman Vetter[1,2] and Dagmar Iber[1,2,*]

ABSTRACT

Tissue patterning during embryonic development is remarkably precise. Here, we numerically determine the impact of the cell diameter, gradient length and the morphogen source on the variability of morphogen gradients. We show that the positional error increases with the gradient length relative to the size of the morphogen source, and with the square root of the cell diameter and the readout position. We provide theoretical explanations for these relationships, and show that they enable high patterning precision over developmental time for readouts that scale with expanding tissue domains, as observed in the *Drosophila* wing disc. Our analysis suggests that epithelial tissues generally achieve higher patterning precision with small cross-sectional cell areas. An extensive survey of measured apical cell areas shows that they are indeed small in developing tissues that are patterned by morphogen gradients. Enhanced precision may thus have led to the emergence of pseudostratification in epithelia, a phenomenon for which the evolutionary benefit had so far remained elusive.

KEY WORDS: Morphogen gradient, Patterning, Precision, Development, Cell size

INTRODUCTION

During embryogenesis, cells must coordinate complex differentiation programs within expanding tissues. According to the French flag model (Wolpert, 1969), morphogen gradients define pattern boundaries in the developing tissue based on concentration thresholds. Exponential functions of the form

$$C(x) = C_0 e^{-x/\lambda} \quad (1)$$

approximate the shape of measured morphogen gradients very well (Kicheva et al., 2007; Gregor et al., 2007; 2008; Yu et al., 2009; Wartlick et al., 2011; 2014; Cohen et al., 2015; Mateus et al., 2020). For such gradients, the mean readout position

$$\mu_x = \text{mean } [x_\theta]$$

and the positional error

$$\sigma_x = \text{stddev } [x_\theta]$$

[1]Department of Biosystems Science and Engineering, ETH Zürich, Mattenstrasse 26, 4058 Basel, Switzerland. [2]Swiss Institute of Bioinformatics, Mattenstrasse 26, 4058 Basel, Switzerland.

*Author for correspondence (dagmar.iber@bsse.ethz.ch)

J.A.A., 0000-0003-0876-3363; R.V., 0000-0003-2901-7036; D.I., 0000-0001-8051-1035

of the domain boundary positions

$$x_\theta = \lambda \ln \frac{C_0}{C_\theta}$$

in different embryos depend on the variation in the decay length λ and in the amplitude C_0 relative to the concentration threshold C_θ. Strikingly, the positional error of measured morphogen gradients has been reported to exceed that of their readouts (Houchmandzadeh et al., 2002; Gregor et al., 2007; Zagorski et al., 2017). Several theories have been proposed to explain the high readout precision, despite inevitable noise and variation in morphogen gradients and their readout processes. They include temporal and spatial averaging, self-enhanced morphogen turnover, the use of opposing gradients, dynamic readouts, and cell-cell signalling (Houchmandzadeh et al., 2002; Gregor et al., 2007; Lander et al., 2009; Morishita and Iwasa, 2009, 2011; Tkačik et al., 2015; Zagorski et al., 2017; Erdmann et al., 2009; Sokolowski and Tkačik, 2015; Ellison et al., 2016; Mugler et al., 2016; Reyes et al., 2022 preprint). In zebrafish, in which cells are rather motile, cell sorting and competition can further enhance boundary precision (Xiong et al., 2013; Akieda et al., 2019; Tsai et al., 2020). Here, we have studied patterning precision conveyed by morphogen gradients in epithelia but leave the effect of precision-enhancing processes in the morphogen readout for future work.

A recently developed numerical framework estimates how much variability in and between morphogen gradients can be accounted for by cell-to-cell variability reported for morphogen production, decay and diffusion (Vetter and Iber, 2022). In this article, we extend the model to take a different perspective on the precision of gradient-based patterning in cellular tissues. We analyse the impact of various length scales present in the epithelium, such as the cell diameter and source size, as well as spatial averaging, on morphogen gradient variability. The findings suggest that positional accuracy is higher, the narrower the cells and the larger the morphogen source.

We approximate the patterning axis by a discrete line consisting of two subdomains, a source domain on the interval $-L_s \leq x \leq 0$ and a patterning domain on the interval $0 \leq x \leq L_p$, each divided into sub-intervals i representing individual epithelial cells with diameter δ_i in 1D, or cross-sectional areas A_i in 2D (Fig. 1A). Noisy exponential gradients were generated by numerically solving the one-dimensional steady-state reaction-diffusion boundary value problem (Vetter and Iber, 2022)

$$p_i H(-x) - d_i C(x) = -D_i \frac{\partial^2 C(x)}{\partial x^2} \quad (2)$$

with zero-flux boundary conditions

$$\left. \frac{\partial C}{\partial x} \right|_{x=-L_s, L_p} = 0.$$

Eqn 2 contains a source with production rates p_i and a linear sink with degradation rates d_i, and models morphogen transport by Fickian diffusion with effective coefficients D_i; subscripts i indicate
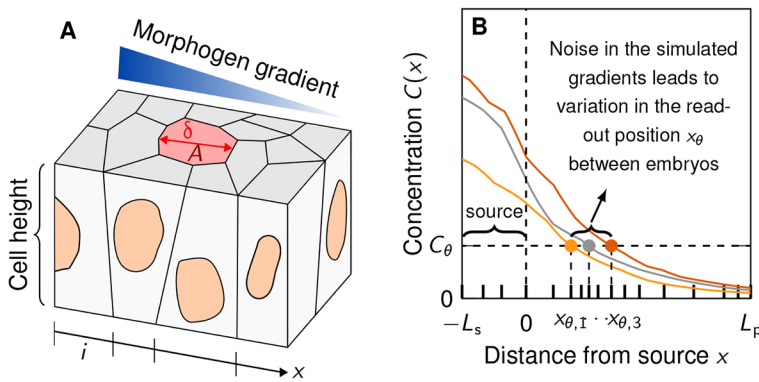
DEVELOPMENT

Fig. 1. Patterning in epithelial tissues with variability in the morphogen kinetics and cell size. (A) Schematic of an epithelial layer of cells (index i) with cross-sectional area A and diameter δ along the patterning axis x. (B) Schematic of positional variability resulting from the readout of noisy gradients in a cellular domain, split into a morphogen-secreting source of length L_s and a patterning domain of length L_p.

that they vary from cell to cell. The Heaviside step function $H(-x)$ ensures that morphogen production occurs only in the source, whereas degradation is assumed to take place over the whole domain. The kinetic parameters $k=p, d, D$ were drawn for each cell independently from log-normal distributions. This assumes statistical independence of neighbouring cells; we will later relax this assumption by introducing spatial correlation. The distributions had prescribed mean values μ_k and respective coefficients of variation $CV_k=\sigma_k/\mu_k$, analogous to Vetter and Iber (2022). We fixed molecular variability at the physiological value $CV_k=0.3$ (Vetter and Iber, 2022).

As a new source of noise, we introduced cell size variability. As the cell area distributions in the *Drosophila* larval and prepupal wing discs, and in the mouse neural tube resemble log-normal distributions (Sánchez-Gutiérrez et al., 2016; Guerrero et al., 2019), we drew individual cell areas A_i independently of a log-normal distribution with a prescribed mean μ_A and a coefficient of variation CV_A. This allowed us to evaluate the impact of cell-to-cell variability in the production, degradation and diffusion rates p_i, d_i and D_i, as well as in the cell cross-sectional areas A_i, on gradient variability (Fig. 1B).

RESULTS

Gradient variability increases with cell size, but not with physiological levels of cell area variability

We quantify relative variability or uncertainty of a positive quantity X by its coefficient of variation $CV_X=\sigma_X/\mu_X$, where μ_X and σ_X indicate the mean and standard deviation of X, respectively. For the local morphogen concentration, this is CV_C. Alternatively, one can fit Eqn 1 to each generated morphogen gradient (see supplementary Materials and Methods) and quantify CV_λ and CV_0 of the two free parameters λ and C_0 individually. We performed simulations covering a wide range of cell sizes, potentially larger than is relevant for a specific type of tissue or organism, to reveal the functional dependency of gradient variability on the cell diameter with statistical confidence. An increase in the average cell diameter μ_δ leads to greater variability in λ and C_0 (Fig. 2A,B), according to power laws

$$CV_\lambda \sim \mu_\delta^\alpha \quad \text{and} \quad CV_0 \sim \mu_\delta^\beta \qquad (3)$$

with exponents $\alpha=0.510\pm0.004$ (SE, Fig. 2A, blue curve) and $\beta=0.472\pm0.005$ (Fig. 2B, blue curve). The amplitude variability CV_0 plateaus when $\mu_\delta \geq L_s$, because the source defaults back to a single cell in this case. Square-root scaling for the decay length variability ($\alpha=1/2$) follows theoretically from the law of large numbers and is consistent with the inverse-square-root scaling reported for the dependency of CV_λ on the patterning domain length

L_p at fixed cell size (Vetter and Iber, 2022). Together, this suggests that

$$CV_\lambda \sim \sqrt{\frac{\mu_\delta}{L_p}} \sim \sqrt{\frac{1}{N_{cells}}} \qquad (4)$$

where N_{cells} is the (mean) number of cells along the patterning axis. Similarly, morphogen sources composed of more and smaller cells buffer cell-to-cell variability in morphogen kinetics more effectively, leading to the observed reduction in amplitude variability CV_0. Smaller cell diameters thus lead to smaller effective morphogen gradient variability.

Cell-to-cell variability in the cross-sectional cell area A does not affect the gradient variability as long as $CV_A<1$ (Fig. 2C,D). Only for extreme cell area variability exceeding 1 does the variability in λ grow (Fig. 2C). However, we are not aware of any reported $CV_A>1$ (Guerrero et al., 2019; Kokic et al., 2019 preprint; Gómez et al., 2021; Bocanegra-Moreno et al., 2023). Consequently, cell size has a considerable impact on gradient variability, while physiological levels of variability in the cell area do not contribute to gradient imprecision. A larger source or gradient length reduces only the amplitude variability, but does not affect the decay length variability (Fig. 2E-H). Amplitude and gradient decay length variability is reduced in a source that is composed of many cells with a small mean diameter (see supplementary Materials and Methods for further details, Fig. S5). The parameter values in all reported simulations correspond to those reported for the mouse neural tube ($\mu_\lambda=20$ μm, $\mu_\delta=5$ μm, $L_s=5\mu_\delta$ and $L_p=50\mu_\delta$), unless stated otherwise. At these values, source sizes above 25 μm and gradient decay lengths above 20 μm barely reduce amplitude variability. Sonic hedgehog (SHH) in the neural tube is secreted from both the notochord and the floor plate, while bone morphogenetic protein (BMP) is secreted from both the ectoderm and the roof plate. Intriguingly, while the SHH-secreting notochord shrinks over time, it still measures about 30 μm in width by the 5-somite stage (Imuta et al., 2014), and the SHH-secreting floor plate then emerges in the ventral part of the neural tube and widens over time (Kicheva et al., 2014). The gradient length remains constant at about $\mu_\lambda=20$ μm (Cohen et al., 2015; Zagorski et al., 2017), the largest value for which the positional error remains small at a large distance ($12\mu_\lambda=240$ μm) from the source. The source size thus assumes the smallest value and the gradient decay length the largest value for which morphogen gradient variability remains small.

Readout position is barely shifted by spatial averaging

As cells can assume only a single fate, domain boundaries must follow cell boundaries (Fig. 3A). We sought to quantify the impact on the readout position if epithelial cells average the signal over
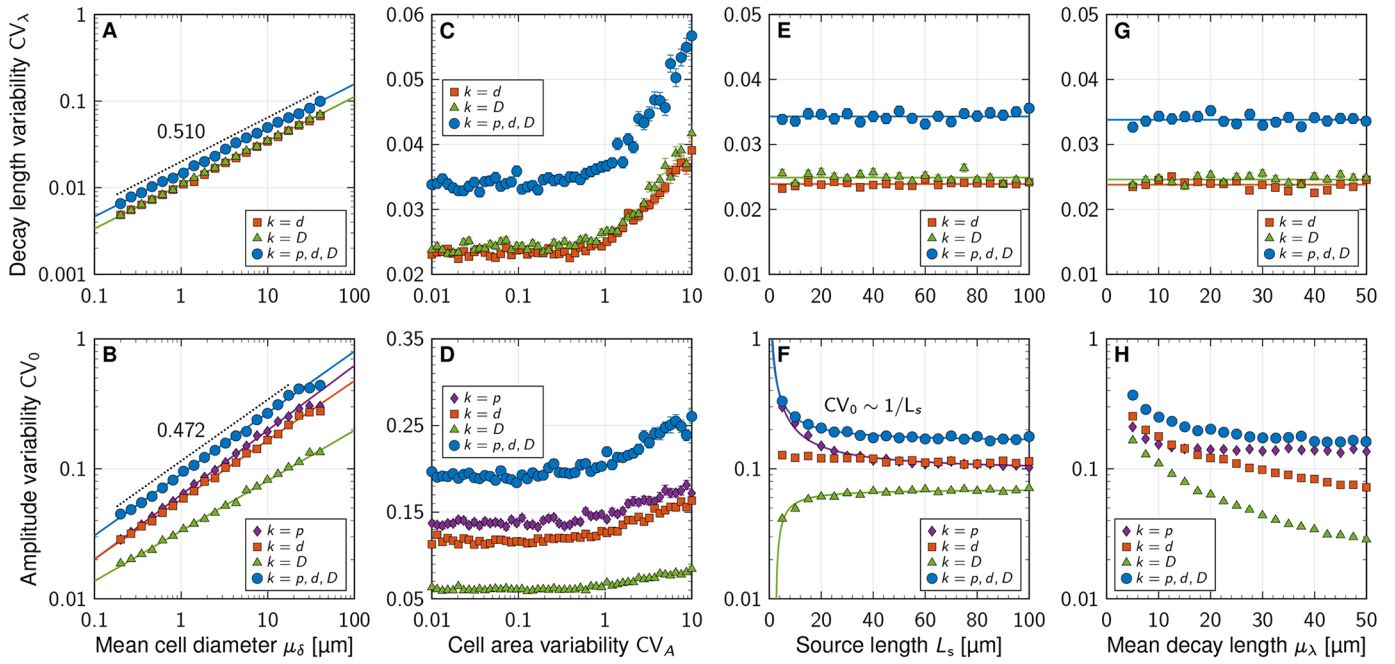
Fig. 2. Impact of cell size, source length and gradient length on morphogen gradient variability. (A,B) Scaling of gradient variability with the cell diameter at fixed kinetic variability $CV_{p,d,D}$ and fixed cell area variability CV_A. Fitted power-law exponents are indicated, and correspond to fits to the blue data points. (C,D) Effect of cell area variability on gradient variability. (E,F) Effect of source length on gradient decay length and amplitude variability. (G,H) Impact of mean gradient decay length on decay length and amplitude variability. Data are mean±s.e.m. of $n=10^3$ independent simulations, with kinetic variability only in the parameters indicated by different symbols: purple, CV_p=0.3, $CV_{d,D}$=0; red, CV_d=0.3, $CV_{p,D}$=0; green, CV_D=0.3, $CV_{p,d}$=0; blue, $CV_{p,d,D}$=0.3. Cell area variability: CV_A=0.5, except in C,D. Domain sizes: L_s=25 µm, except in E,F; L_p=250 µm, except in F,G. The effect of CV_p on CV_λ is minuscule, $\mathcal{O}(10^{-8})$, and therefore not plotted in the top row. See supplementary Materials and Methods for further details and Table S1 for fit parameters.

their entire apical cell surface. Assuming that cells have no orientational bias, we can approximate cell surfaces as disks with radius $r=\mu_\delta/2$ about a centre point x_0. If threshold-based readout operates on the averaged concentration, the effective readout domain boundary is shifted along the exponential concentration gradient to $x_0=x_\theta+\Delta x$ by the distance

$$\Delta x = \lambda \ln \left[\sum_{k=0}^{\infty} \frac{(r/2\lambda)^{2k}}{k!(k+1)!} \right]$$
$$= \lambda \left[\frac{1}{8} \left(\frac{r}{\lambda} \right)^2 - \frac{1}{384} \left(\frac{r}{\lambda} \right)^4 + \mathcal{O}\left(\left(\frac{r}{\lambda} \right)^6 \right) \right] \quad (5)$$

in absence of morphogen gradient variability and cell size variability (see supplementary Materials and Methods for further details, Fig. S1). For $r=2.45$ µm and $\lambda=19.3$ µm, as found for SHH in the mouse neural tube (Cohen et al., 2015), the shift is $\Delta x=0.039$ µm or 0.8% of the cell diameter.

In the case of rectangular rather than circular cell areas, cells are confined to the interval $[x_0-r, x_0+r]$. The theoretically predicted shift is then approximately 0.052 µm in the mouse neural tube (see supplementary Materials and Methods for further details, Fig. S2) or 1% of the cell diameter. This agrees with the shift we measured in our simulations, $\Delta x=0.0523\pm0.0001$ µm (mean±s.e.m.), confirming that spatial averaging of an exponential gradient results in a higher average concentration than centroid readout. Kinetic and area variability both increase Δx (Fig. 3B), but it remains small enough (small fractions of a cell diameter) to be neglected in the analysis of tissue patterning under biological conditions where $r/\lambda \ll 1$. Linear gradients (Wolpert, 1969) would not result in any shift at all.

Spatial averaging barely reduces variability between gradients

Spatial and temporal averaging can reduce the positional error of morphogen gradients (Berg and Purcell, 1977). Previously, these
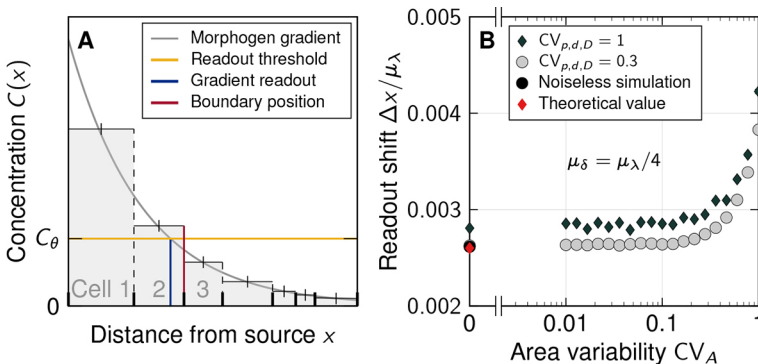

Fig. 3. Readout position of exponential gradients is barely shifted by spatial averaging. (A) Cell-based readout of a morphogen gradient. A concentration threshold C_θ (yellow) defines a readout position x_θ (blue). If cells read out cell area averaged concentrations, the effectively sensed concentration profile is a step function (grey). Pattern boundaries form at cell edges (red). For illustrative purposes, the cell size is exaggerated compared with the gradient decay length. (B) Cell-area-averaged readout of exponential gradients results in a small shift, Δx, compared with readout at the cell centroid.

mechanisms have been mainly analysed at the level of the morphogen readouts – typically transcription factors (TFs) – which are averaged by diffusion between nuclei (Houchmandzadeh et al., 2002; Bialek and Setayeshgar, 2005; Gregor et al., 2007; Erdmann et al., 2009; Sokolowski and Tkačik, 2015; Ellison et al., 2016; Mugler et al., 2016). This is easily possible in a syncytium, as present in the early *Drosophila* embryo, but the role of TF diffusion in increasing patterning precision has remained controversial (Jaeger and Verd, 2020). In an epithelium, nuclei are separated by cell membranes such that the averaging of morphogen-induced factors would require transport between cells, a complex and slow process with many additional sources of molecular noise (Entchev and González-Gaitán, 2002; Lander et al., 2002). However, epithelial cells potentially can reap the benefits of spatial averaging by averaging the morphogen signal over their surface (Fig. 4A, green). Receptors may either be dispersed on the apical cell surface or along the baso-lateral surface, or, in the case of hormones, be limited to nuclei (Saitoh et al., 2013; Zhang et al., 2019). In the last case, morphogen receptors would be limited to a small patch, which could either be randomly positioned (Fig. 4A, blue) or located at the centroid of the cell (Fig. 4A, red). In the mouse neural tube, the SHH receptor PTCH1 is restricted to a cilium located on the apical surface (Saade et al., 2013). The range of spatial averaging then depends on the cilium length and flexibility, rather than the cross-sectional cell area (Fig. 4A, purple). We sought to analyse how the different spatial averaging strategies without crosstalk between neighbouring cells affect the variability of gradients and thus the positional error.

Although the mean cell diameter μ_δ greatly affects the concentration variability CV_C, the readout strategy has only a moderate impact (Fig. 4B). The difference is most pronounced for large cells ($\mu_\delta=\mu_\lambda$),

where the sensed morphogen variability is largest if the cellular readout point is randomly placed (Fig. 4B, blue). Readout at the centroid or averaged over the entire cell yield similar sensed concentration variabilities. This is understandable because the theoretical considerations above predict only a small shift. In addition, a cilium that averages the gradient concentration over larger regions than a single cell area barely reduces the sensed variability (Fig. 4C).

In summary, larger cross-sectional cell diameters increase the variability of the morphogen concentration profiles, while spatial averaging over the cell surface barely reduces the gradient variability. Spatial averaging may, however, counteract detection noise at low morphogen concentrations far away from the source. It is currently unknown over what distance morphogen gradients operate. At a distance 12λ from the source, for example, exponential concentrations will have declined by $e^{12}\approx160$-thousand-fold. At such low levels, detection noise may dominate readout variability unless removed by spatial averaging.

Scaling of the positional error with gradient length, source size, cell diameter and readout position

From dimensional analysis, the positional error of the gradient, σ_x, being a measure of distance, must scale with a multiplicative combination of the length scales occurring in the patterning process. These can either originate from geometrical features of the tissue or from the reaction-diffusion kinetics. We varied all relevant length scales in simulations and found that σ_x is asymptotically proportional to the mean characteristic gradient decay length, μ_λ, close to the source, but transitions to μ_λ^2 at larger distances (Fig. 4D). Additionally, it is inversely proportional to the source length L_s, asymptotically for small L_s (Fig. 4E), but saturates for large sources.
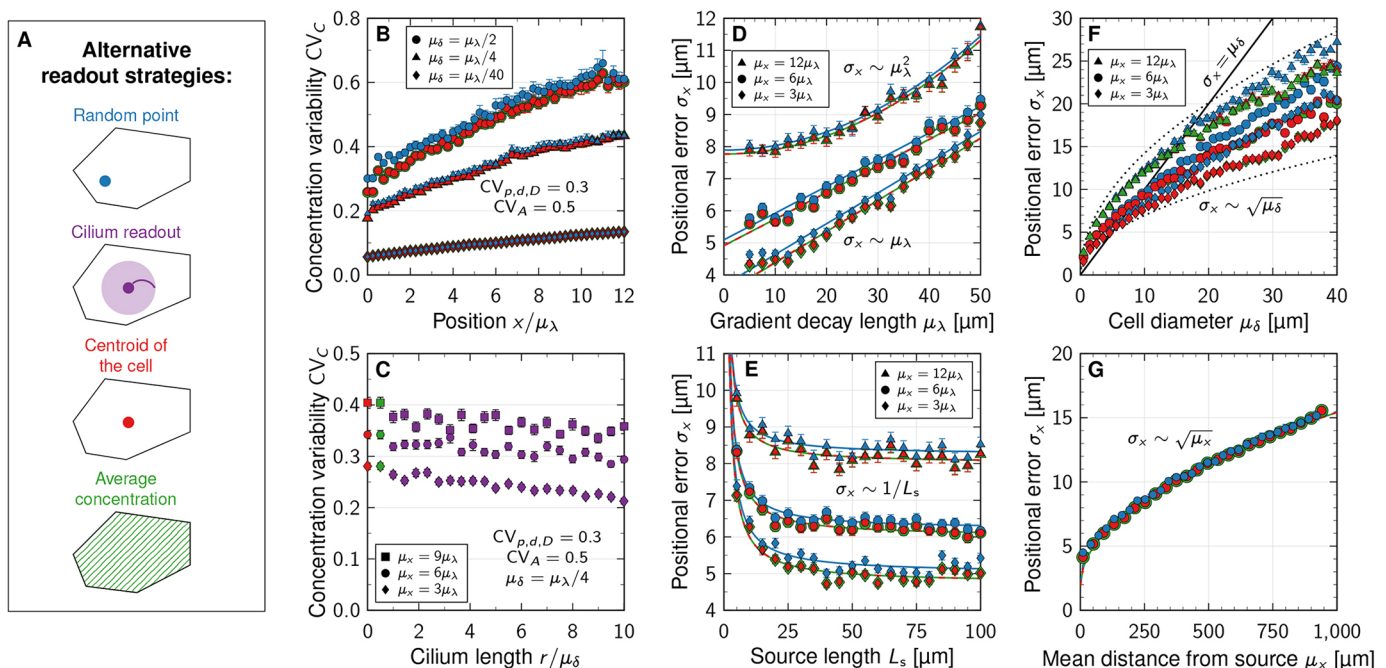

Fig. 4. Impact of spatial averaging, gradient length, source size, cell diameter and readout position on the positional error of morphogen gradients. (A) Four different methods to explain how cells may read out morphogens. Colours in B-G correspond to these readout mechanisms. (B) Concentration variability along the patterning domain for different readout mechanisms and different cell sizes. (C) Effect of spatial averaging over a readout region with radius *r* on sensed morphogen concentration variability. (D) Impact of absolute gradient decay length μ_λ on the positional error. (E) Impact of source size L_s on the positional error. (F) Effect of mean cell diameter μ_δ on the positional error. Dotted lines show the relationship $\sigma_x = \gamma\sqrt{\mu_\delta}$ for γ=2.2, 4.5 (lengths in units of µm). (G) Scaling of the positional error with the readout position μ_x. Scaling relationships in D-G are asymptotic. Each data point in B-G corresponds to the mean±s.e.m. of $n=10^3$ independent simulations. Simulation parameters: $L_p=65\mu_\delta$, except in G; $\mu_\lambda=20$ µm, except in D; $L_s=5\mu_\delta$, except in E; $m\mu_\delta=5$ µm, $CV_{p,d,D}=0.3$, $CV_A=0.5$. See supplementary Materials and Methods for further details and Table S1 for fit parameters.

Moreover, the positional error increases with the square root of the mean cell diameter μ_δ (Fig. 4F) and, up to an offset, with the square root of the mean position along the patterning axis μ_x (Fig. 4G). Together, this can be expressed by the asymptotic scaling relationship

$$\sigma_x \sim \frac{\mu_\lambda}{L_s} \sqrt{\mu_\delta \, \mu_x}. \qquad (6)$$

The linear dependency on the gradient length μ_λ is due to the effect of gradient steepness on the positional error, and outweighs the reduction in gradient amplitude variability (Fig. 2H). It intuitively follows from $\sigma_x \approx |\partial C/\partial x|^{-1} \sigma_C \approx \mu_\lambda \mathrm{CV}_C$, which is a valid approximation when the average gradient has an exponential shape (Vetter and Iber, 2022). As before (Fig. 2F), at constant μ_δ, a longer source reduces the gradient amplitude variability because noise is buffered by a larger number of source cells (see supplementary Materials and Methods for further details, Fig. S5). Narrower cells (smaller μ_δ) reduce the positional error of the morphogen gradients according to the law of large numbers, $\sigma_x \sim \sqrt{\mu_\delta}$. Cell width in the patterning domain is more influential than in the source, however, and the benefit of reducing cell width in the source alone is limited (see supplementary Materials and Methods for further details, Fig. S6). The deterministic limit ($\mathrm{CV}_C \to 0$, $\sigma_x \to 0$) is recovered in the continuum limit $\mu_\delta \to 0$. Domain boundaries can thus be defined more accurately at a certain target location μ_x within the tissue with narrow cells. Depending on the other lengths, the positional error can easily be less than a cell diameter if the readout position is close enough to the source (Fig. 4F). We note that the previously reported linear scaling $\sigma_x \sim \mu_x$ (Vetter and Iber, 2022) is valid only for idealized gradients that vary only through noise in λ, but not in their amplitude or from cell to cell. For the noisy more-physiological gradients simulated here, the positional error increases according to $\sigma_x \sim \sqrt{\mu_x}$ (asymptotically, Fig. 4G) and thus remains lower with increasing distance from the source than previously anticipated. This further challenges previous reports of excessive inaccuracy of the SHH and BMP gradients in the mouse neural tube (Zagorski et al., 2017).

High precision of scaled patterns by parallel changes in gradient length, source size and cell diameter in the *Drosophila* wing disc

The Decapentaplegic (Dpp) morphogen gradient in the *Drosophila* wing imaginal disc defines the position of several veins in the adult wing (Fig. 5A). Thus, the anterior-most limits of the Dpp source and the Dpp target gene spalt (*sal*) define the positions of the third (L3) and second (L2) longitudinal veins in the anterior compartment, respectively (Sturtevant et al., 1997; Bollenbach et al., 2008; Restrepo et al., 2014; Tripathi and Irvine, 2022), while the fifth longitudinal (L5) wing vein forms at the border between the expression domains of optomotor-blind (*omb*) and brinker (*brk*) in the posterior compartment (Cook et al., 2004). The Dpp readout positions scale with the total length of the uniformly expanding patterning domain, such that the anterior position of the Sal-domain boundary remains roughly at 40-45% of the anterior domain length L_a, while the posterior Omb domain boundary remains at approximately 50% of the posterior domain length L_p (Bollenbach et al., 2008; Wartlick et al., 2011; Hamaratoglu et al., 2011; Restrepo et al., 2014). The gradient readout positions scale with the length of the patterning domain, because both the gradient length, λ, and the gradient amplitude, C_0, increase dynamically with the expanding tissue (Wartlick et al., 2011; Hamaratoglu et al., 2011; Fried and Iber, 2014, 2015) (Fig. 5B). On their own, the increases in μ_λ and in μ_x would lower the precision of the

readout substantially over time (Eq. 6). However, the Dpp source widens in parallel, keeping the μ_λ/L_s ratio at about 0.69 (Fig. 5B). Moreover, the apical cell diameter μ_δ shrinks threefold close to the source from 4.5 to 1.5 µm (Aegerter-Wilmsen et al., 2012; Corrigall et al., 2007; Escudero et al., 2011; Legoff et al., 2013; Kokic et al., 2019 preprint), which somewhat balances the increase in μ_x over time. Plugging these dynamics into our model, the simulations showed that the positional error at $\mu_x = 0.4 L_a$ increases from 2.9 µm to 4.3 µm over developmental time (Fig. 5C, orange diamonds). If no compensation were taking place, the positional error would increase to about 6.5 µm in the same time period (Fig. 5C, blue circles).

The relative patterning precision, as quantified by the coefficient of variation $\mathrm{CV}_x = \sigma_x/\mu_x$, has even been reported to increase during development, as the CV of the distance between the L2 and L3 veins in the adult fly is only half ($\mathrm{CV}_x = 0.08$) that of the anterior-most Sal domain boundary ($\mathrm{CV}_x = 0.16$) (Bollenbach et al., 2008). How this increase in precision is achieved has remained elusive. In light of Eqn 6, $\mathrm{CV}_x = \sigma_x/\mu_x \sim 1/\sqrt{\mu_x}$ (Fig. 5D), such that the decreasing CV_x in adult stages could at least partly be a consequence of the increase in $\mu_x = 0.4 L_a$ between the stage when the precision of the Sal domain boundary was measured and the termination of Dpp-dependent patterning. The asymptotic relationship $\sigma_x \sim \sqrt{\mu_x}$ may thus provide an explanation of how the relative precision of patterning increases during *Drosophila* wing disc development.

The effect of spatial correlation
Our theoretical considerations and simulations above are based on statistical independence between adjacent cells. To examine the effect of spatial correlations, we performed additional simulations in which this assumption was relaxed. We introduced a maximal degree of spatial correlation between neighbouring cells, given a certain degree of intercellular variability CV_k, by sorting the kinetic parameters p_i, d_i and D_i in ascending or descending order along the patterning axis after they had been drawn from their respective probability distributions, and then solved the reaction-diffusion problem (Eqn 2). The square-root increase of the positional error with the mean cell diameter remains intact in the presence of such spatial correlations between cells (see supplementary Materials and Methods for further details, Fig. S3), with a slightly smaller prefactor. Because any physiological level of cell-to-cell correlation that preserves CV_k will lie somewhere between the uncorrelated and the maximally correlated extremes, the impact of such a form of spatial correlation on patterning precision can be expected to be minimal, and our findings also remain valid in presence of spatial correlations.

An additional form of inter-cellular correlation may occur if nearby cells stem from the same lineage and, as such, may have correlated kinetic properties. In its most extreme form, neighbouring cells may share all their molecular parameters, p, d and D, effectively becoming one wider joint cell in our model. We can use our results for cell-autonomous noise to predict the dependency of patterning precision on the number of adjacent cells sharing their kinetic properties, N. As the effective cell diameter simply becomes $N\mu_\delta$, the positional error will scale as $\sigma_x \sim \sqrt{N}$. In this sense, the mean cell diameter μ_δ in our formulas may be interpreted as an effective spatial distance over which morphogen kinetics are shared, proportional to a spatial correlation length in the tissue, if any.

Cell-specific morphogen production and decay rates, and local variability in morphogen transport rates have not yet been quantified in epithelial tissues. A spatial coupling of molecular noise in dividing cells would require a perfectly symmetric division of cell contents upon cell division and the absence of cell-intrinsic noise. Dpp-containing endosomes are indeed distributed equally upon cell
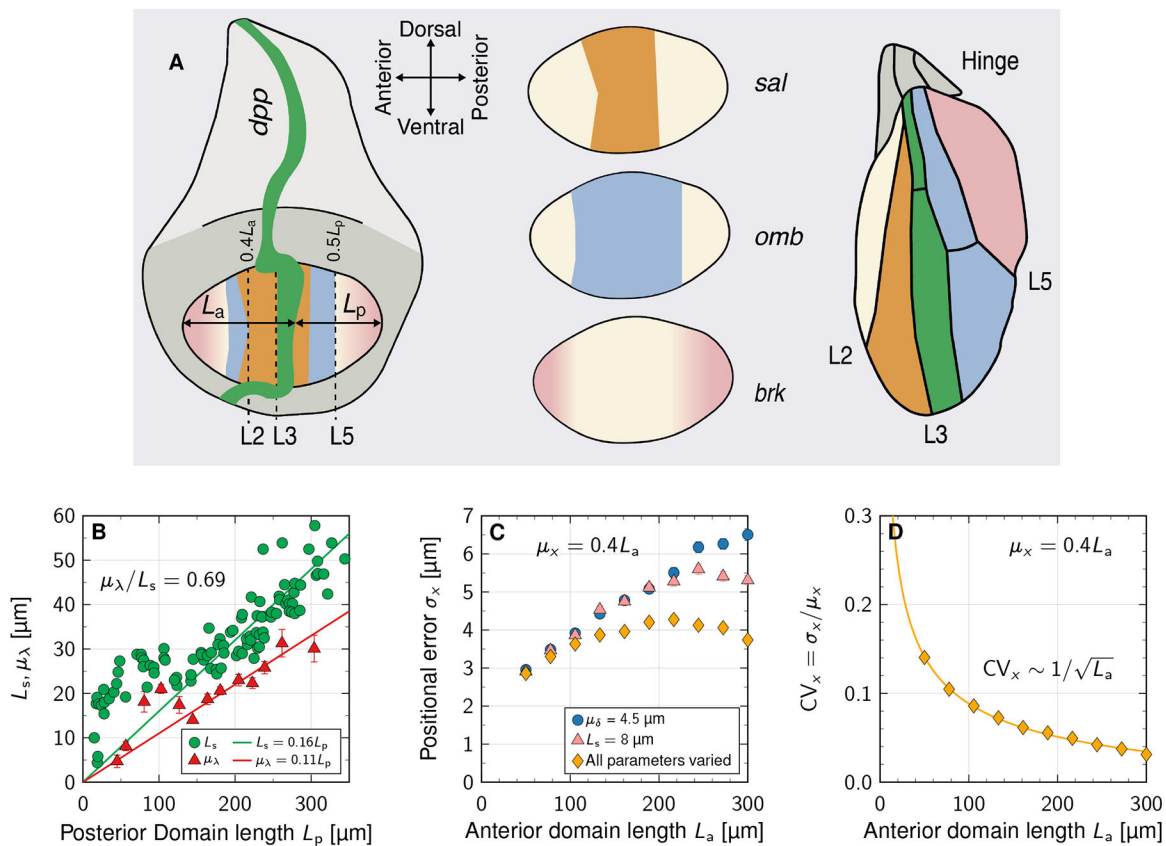
Fig. 5. High precision of scaled patterns by parallel changes of gradient length, source size and cell diameter in the *Drosophila* wing disc.
(A) Schematic of Dpp-dependent patterning in the *Drosophila* wing disc (adapted, with permission, from Matsuda et al., 2021, where it was published under a CC-BY 4.0 license). Dpp is secreted from the green stripe, and supports the expression of *sal* (orange) and *omb* (blue), while repressing *brk* (pink) in the pouch. The colours in the wing blade indicate the gene that defines the particular vein: the anterior-most limit of the *sal* domain defines the position of the L2 vein, the anterior-most limit of the *dpp* domain the L3 vein and the posterior-most limit of the *omb* domain define the L5 vein. *omb* is also expressed in the anterior *sal* domain, and *sal* in part of the posterior *omb* domain, but these are omitted from the wing blade for clarity. For further details, see the main text. (B) The reported Dpp gradient length and source size increase in parallel with the expanding length, L_p, of the posterior compartment. Data are from Wartlick et al. (2011). (C) The predicted positional error at the relative readout position $\mu_x/L_a=40\%$ is smallest when μ_λ and L_s evolve according to the linear fits in B, and μ_δ declines linearly from 4.5 to 1.5 µm (orange diamonds). The positional error if μ_δ is fixed and μ_λ, L_s evolve (blue circles), or if the source length is fixed and μ_λ, μ_δ evolve (pink triangles) is shown for comparison. (D) The predicted positional coefficient of variation $CV_x=\sigma_x/0.4L_a$ declines as the domain expands. See supplementary Materials and Methods for further details and Table S1 for fit parameters.

division in the *Drosophila* wing disc (Bökel et al., 2006). However, no cellular system without intrinsic noise has so far been reported. Differences between genetically identical sister cells were first shown for bacterial cells (Elowitz et al., 2002), but have since also been demonstrated for mammalian cells, and pose a key challenge in synthetic biology (Raser and O'Shea, 2005; Zoller et al., 2015; Urban and Johnston, 2018). The coefficients of variation that we used are based on the reported variabilities of production and decay rates in single genetically identical cells in cell culture (Vetter and Iber, 2022).

There are further reasons why low spatial correlation of the kinetic parameters is to be expected. In pseudostratified epithelia, interkinetic nuclear migration (IKNM) introduces differences between cells as the cell cross-sectional areas change along the entire apical-basal axis over time (Gómez et al., 2021). As the tight junctions constitute a diffusion barrier between the apical and the basolateral domains, the apical receptor density between cells will change dynamically between cells if the apical receptor number is equal and fixed for all cells. To maintain the same receptor density, even though IKNM proceeds at different rates between neighbouring cells, as reflected in the different nuclear positions along the apical-basal axis (Gómez et al., 2021), the processes that

balance receptor production and internalisation would need to be identical between neighbouring cells, although differences in cell and nuclear volumes may also need to be compensated for. The same holds for the glyocalyx and extracellular matrix, which define the speed of morphogen diffusion, or for fillipodia, in the case of cytoneme-based transport. In summary, the combination of an unequal distribution of cell components in cell division, differences in the relative surface area to cell and nuclear volume, and intrinsic noise in gene expression must be expected to lead to individual differences between neighbouring cells, even if they stem from the same lineage.

Epithelial tissues patterned by morphogen gradients have small mean apical cell areas

After finding that patterning precision is greater with narrower cells in our model, we collected mean apical cell areas for a wide range of tissues from the literature to check whether cell diameters are small in tissues that rely on gradient-based patterning (Fig. 6). In the chick (cNT) and mouse neural tube (mNT), where SHH, BMP and WNT gradients define the progenitor domain boundaries (Briscoe and Small, 2015), the mean apical cell areas are largely around 7 µm²
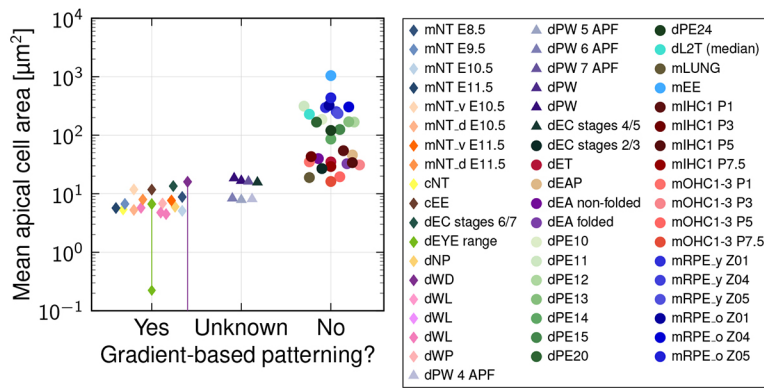
Fig. 6. Mean apical cell areas of epithelial tissues. Apical cell areas were categorised into three groups based on whether the tissue is patterned by morphogen gradients or not, or whether this is not known. m, mouse; d, *Drosophila*; c, chick (see text for details).

and remain below 12 µm² (Escudero et al., 2011; Guerrero et al., 2019; Bocanegra-Moreno et al., 2023). The chick embryonic ectoderm (cEE) appears to be patterned by BMP gradients (Pera et al., 1999), with mean apical cell area just below 12 µm² (Escudero et al., 2011). In the *Drosophila* larval eye disc (dEYE), notum (dNP) and wing disc (dWL), Hedgehog (Hh), Decapentaplegic (Dpp) and Wg gradients pattern the epithelium (Tomoyasu et al., 2000; Cavodeassi et al., 2002; Briscoe and Small, 2015), with mean apical cell areas smaller than 7 µm² (Corrigall et al., 2007; Escudero et al., 2011; Aegerter-Wilmsen et al., 2012; Kokic et al., 2019 preprint). The mean apical cell areas of the wing disc increase through the pre-pupal stages (dWP and dPW), to approximately 18 µm² in the pupal stages (Escudero et al., 2011; Kokic et al., 2019 preprint); other measurements in the *Drosophila* wing disc (dWD) report mean apical cell areas from 0 to 16 µm² (Aegerter-Wilmsen et al., 2012). In the *Drosophila* eye antennal disc, no gradient-based patterning was described (dEA folded, mean apical cell areas of approximately 33 µm²; dEA non-folded, mean apical cell areas of approximately 39 µm²) (Ku and Sun, 2017). For the peripodal membrane (dPE10-24) of the *Drosophila* eye disc, no gradient-based patterning has been described and mean apical cell areas range from 85 µm² to more than 300 µm² (Kokic et al., 2019 preprint). In the *Drosophila* egg chamber (dEC), the mean apical cell areas decline from around 30 µm² at stage 2/3 to around 10 µm² by stage 6/7 (Finegan et al., 2019), consistent with reported gradient-based patterning at stage 6 (Osterfield et al., 2017); we did not find reports of earlier gradient-based patterning. Although gradients pattern the *Drosophila* blastoderm syncytium (Briscoe and Small, 2015), we are not aware of morphogen gradient readout during cellularisation. In the *Drosophila* embryo anterior pole (dEAP), the mean apical cell area is approximately 46 µm² and in the embryo trunk (dET) it is roughly 35 µm² (Rupprecht et al., 2017), much larger than in the neural tube or wing disc. Before cellularisation, the situation is different from that in an epithelium in that free diffusion in the inter-nuclear space of the syncytium likely counteracts any sharp transition in the kinetic parameters, as represented in our epithelial model, where cell membranes compartmentalise space. In the *Drosophila* L2 trachea (dL2 T), no gradients have been reported and the mean apical cell areas are greater than 200 µm² (Skouloudaki et al., 2019). In the mouse embryonic lung (mLUNG), no morphogen gradients have been reported, despite chemical patterning (Iber, 2021), and the mean apical cell area is approximately 19 µm² (Kadzik et al.,2014). Mean apical cell areas in the postnatal (P1-P21) cochlea are between 15 and 55 µm² (Etournay et al., 2010). In adult mouse retinal pigment epithelial (mRPE) cells, the mean apical cell areas exceed 200 µm² in young mice (P30) and increase to over 400 µm² in old mice (P720) (Kim et al., 2021). No gradient-based patterning has

been reported in mouse outer hair cells (mOHC1-3; P1, P3, P5, P7.5); mean apical cell areas decrease from 35 µm² (P1) to 16 µm² (P7.5). No gradient-based patterning takes place in the inner hair cells (mIHC1; P1, P3, P6, P7.5); mean apical cell areas decrease from 54 µm² (P1) to 29 µm² (P7.5) (Etournay et al., 2010). No gradient-based patterning has been reported in the mouse ear epidermis (mEE), with mean apical cell areas of 1044 µm² (Yokouchi et al., 2016). The data thus confirm that apical cell areas are small in tissues that employ gradient-based patterning. Our theory makes no prediction about the apical areas in tissues that do not employ gradient-based patterning, but in all cases that we have checked, apical areas are larger and appear to further increase in later developmental stages and in adult animals.

DISCUSSION

We have shown that gradient precision decreases with increasing cross-sectional area of the patterned cells. Consistent with our prediction, apical surface areas are small in epithelia that employ gradient-based patterning. In curved domains, spatial precision will be higher on the inside, where the average cell diameter is smaller. In the mouse neural tube, the SHH-sensing cilium is indeed located on the inner, apical surface (Saade et al., 2013), while in the flat *Drosophila* imaginal discs, cells sense Hedgehog along the entire apical-basal axis (Gore et al., 2021). In the *Drosophila* wing disc, the apical cell diameters shrink in the centre of the domain, such that the apical areas are almost twofold smaller close to the source and increase roughly linearly (Corrigall et al., 2007; Widmann and Dahmann, 2009; Legoff et al., 2013; Bai et al., 2013). In the eye disc, the size gradient is even more pronounced, with tiny apical areas in the Dpp secreting morphogenetic furrow (Corrigall et al., 2007). The declining apical cell diameters have previously been attributed to a mechanical pressure feedback caused by growth (Hufnagel et al., 2007; Aegerter-Wilmsen et al., 2012). However, signalling by Dpp, the fly homolog of mammalian BMP2/4, has been shown to result in taller cells with smaller cross-sectional area in its patterning domain compared with other parts of the *Drosophila* wing and eye disc (Corrigall et al., 2007; Widmann and Dahmann, 2009; Legoff et al., 2013; Bai et al., 2013). Similarly, the morphogens SHH and WNT have been observed to increase cell height and reduce the cell cross-sectional area via their impact on actin polymerisation, myosin localisation and activity in the embryonic mouse neural tube and lung (Kadzik et al., 2014; Widmann and Dahmann, 2009; Gritli-Linde et al., 2002; Kondo and Hayashi, 2015; Chiang et al., 1996). Complementary to these observations, it would be interesting to test our hypothesis in experiments that alter cell shape using either a genetic or mechanical approach (Neufeld et al., 1998; Duda et al., 2019).

In light of our study, it is possible that the morphogen-dependent reduction in the cross-sectional cell area via positive modulation of cell height serves to enhance patterning precision. The precision advantage of small cell diameters may then have led to the emergence of pseudostratification in epithelial monolayers, a phenomenon that has so far remained unexplained. Our finding that wide cells and very large cell area variability are both detrimental to patterning precision indicate that there is potentially a window for epithelial pseudostratification in which patterning precision is optimal: High cell density benefits precision because cell diameters are small; however, with nuclei much wider than the average cell diameter (Gómez et al., 2021), precision would decline due to large area variability. It is remarkable that all the tissues we analysed seem to lie in the optimal range of this trade-off (Kokic et al., 2019 preprint).

We have revealed scaling relationships between the positional error, cell diameter, gradient decay length and source length (Eqn 6). In follow-up work, we found that these also hold for non-exponential gradients arising from non-linear morphogen degradation (Adelmann et al., 2023), as far as they were studied, and also in 2D tissue patterning (Long et al., 2023 preprint). These relationships predict that morphogen gradients remain highly accurate over very long distances, providing precise positional information even at a distance from the morphogen source. Our results are system-agnostic, and could thus apply widely in development. The compensation between cell diameter, gradient length, source size and readout location, which we have found here, allows a patterning system to tune its length scales to achieve a particular level of spatial precision. Our theoretical work suggests a potential evolutionary benefit for a developmental mechanism that regulates features such as the cell diameter or the λ/L_s ratio to maintain high patterning precision. A loss in precision due to a shift in readout position away from the morphogen source, for example, can be compensated for by narrower cells in the source or in the patterning domain. This allows developmental systems to maintain high patterning precision at readout positions that scale with a growing tissue domain.

Whether pre-steady-state gradients, as likely play a role in the patterning of the *Drosophila* wing disc (Fried and Iber, 2014), follow the same behaviour as discovered here for the steady state, remains an issue for future research. Assuming that they do, our results offer a potential explanation for the observed increase in relative patterning precision during wing disc development.

MATERIALS AND METHODS
Generation of variable morphogen gradients
The patterning axis was constructed as follows: a random cell area A_i was drawn for cell i=1, and then converted to a diameter $\delta_i = 2\sqrt{A_i/\pi}$, which assumes that cell surfaces are roughly isotropic. This process was repeated for the next cells i=2, 3,... until their cumulated diameters matched the domain length L_s or L_p. To control the mean cell diameter μ_δ, cell areas were drawn with a mean value of $\mu_A = \pi(\mu_\delta/2)^2(1 + CV_A^2)^{1/4}$ for given μ_δ and CV_A, as follows from the transformation properties of log-normal random variables, such that $\mu_\delta = E[\delta_i] = 2E[\sqrt{A_i}]/\sqrt{\pi}$. The patterning axis was then discretized into subintervals of length δ_i; the source and patterning domains were pasted together, such that x=0 marked the source boundary; random kinetic parameters p_i, d_i and D_i were drawn independently for each cell from log-normal distributions. The results reported in this work are largely independent of the specific choice of probability distribution, given that they do not allow for very small (or even negative) kinetic parameters, which would not be compatible with a successful morphogen transport and patterning process. A gamma distribution with the same mean and variance, for example, yields largely unchanged behaviour (see supplementary Materials and Methods for further details, Fig. S4).

We then solved Eqn 2 numerically on the discretized domain using Matlab's built-in fourth-order boundary value problem solver `bvp4c` (version R2020b). Continuity of the morphogen concentration and its flux was imposed at each cell boundary. Further technical details can be found in Vetter and Iber (2022). Each simulation was repeated n=10^3 times with independent random parameters and cell areas.

Gradient parameter extraction
We determined the amplitude C_0 and decay length λ for each numerically generated noisy morphogen gradient by fitting the deterministic solution to it. With no-flux boundaries, the gradient shapes are hyperbolic cosines that slightly deviate from a pure exponential at the far end (Vetter and Iber, 2022). We fitted these inside the patterning domain to obtain C_0 and λ after logarithmisation of the morphogen concentration, as detailed by Vetter and Iber (2022).

As the fitted characteristic gradient length λ drifts away from the prescribed value for noisy gradients depending on which of the kinetic parameters is varied and by how much (Vetter and Iber, 2022), we corrected for this drift in our numerical implementation to be able to use the true observed value of μ_λ in our results:

$$\mu_\lambda = \lambda(1 + 0.435CV_d^2)^{-0.080}$$
$$\mu_\lambda = \lambda(1 - 0.003CV_D + 1.045CV_D^2 - 0.113CV_D^3 + 0.0043CV_D^4)^{0.471}$$
$$\mu_\lambda = \lambda(1 - 0.011CV_{p,d,D} + 1.355CV_{p,d,D}^2 - 0.179CV_{p,d,D}^3 + 0.0077CV_{p,d,D}^4)^{0.357}$$

where λ is the deterministic (prescribed) value. When only the production rate p was varied, μ_λ=λ. These empirical relationships approximate the data shown by Vetter and Iber (2022).

Author contributions
Conceptualization: R.V., D.I.; Methodology: R.V.; Software: J.A.A., R.V.; Formal analysis: R.V.; Investigation: J.A.A., R.V., D.I.; Data curation: D.I.; Writing - original draft: J.A.A., R.V., D.I.; Writing - review & editing: J.A.A., R.V., D.I.; Visualization: R.V.; Supervision: R.V., D.I.; Project administration: D.I.; Funding acquisition: D.I.

Data availability
This study did not produce new data. The source code is released under the 3-clause BSD license and is deposited in GitLab (https://git.bsse.ethz.ch/iber/Publications/2022).

Peer review history
The peer review history is available online at https://journals.biologists.com/dev/lookup/doi/10.1242/dev.201702.reviewer-comments.pdf

References
Adelmann, J. A., Vetter, R. and Iber, D. (2023). Patterning precision under non-linear morphogen decay and molecular noise. *Elife* **12**, e84757. doi:10.7554/eLife.84757

Aegerter-Wilmsen, T., Heimlicher, M. B., Smith, A. C., De Reuille, P. B., Smith, R. S., Aegerter, C. M. and Basler, K. (2012). Integrating force-sensing and signaling pathways in a model for the regulation of wing imaginal disc size. *Development* **139**, 3221-3231. doi:10.1242/dev.082800

Akieda, Y., Ogamino, S., Furuie, H., Ishitani, S., Akiyoshi, R., Nogami, J., Masuda, T., Shimizu, N., Ohkawa, Y. and Ishitani, T. (2019). Cell competition corrects noisy Wnt morphogen gradients to achieve robust patterning in the zebrafish embryo. *Nat. Commun.* **10**, 4710. doi:10.1038/s41467-019-12609-4

Bai, L., Widmann, T., Jülicher, F., Dahmann, C. and Breen, D. (2013). 3D surface reconstruction and visualization of the *Drosophila* wing imaginal disc at cellular resolution. *Proc. SPIE.* **8654**, 86540D. doi:10.1117/12.2008497

Berg, H. C. and Purcell, E. M. (1977). Physics of chemoreception. *Biophys. J.* **20**, 193-219. doi:10.1016/S0006-3495(77)85544-6

Bialek, W. and Setayeshgar, S. (2005). Physical limits to biochemical signaling. *Proc. Natl. Acad. Sci. USA* **102**, 10040-10045. doi:10.1073/pnas.0504321102

Bocanegra-Moreno, L., Singh, A., Hannezo, E., Zagorski, M. and Kicheva, A. (2023). Cell cycle dynamics controls fluidity of the developing mouse neuroepithelium. *Nat. Phys.* doi:10.1038/s41567-023-01977-w

Bökel, C., Schwabedissen, A., Entchev, E., Renaud, O. and González-Gaitán, M. (2006). Sara endosomes and the maintenance of Dpp signaling levels across mitosis. *Science* **314**, 1135-1139. doi:10.1126/science.1132524

Bollenbach, T., Pantazis, P., Kicheva, A., Bökel, C., González-Gaitán, M. and Jülicher, F. (2008). Precision of the Dpp gradient. *Development* **135**, 1137-1146. doi:10.1242/dev.012062

Briscoe, J. and Small, S. (2015). Morphogen rules: design principles of gradient-mediated embryo patterning. *Development* **142**, 3996-4009. doi:10.1242/dev.129452

Cavodeassi, F., Rodríguez, I. and Modolell, J. (2002). Dpp signalling is a key effector of the wing-body wall subdivision of the *Drosophila* mesothorax. *Development* **129**, 3815-3823. doi:10.1242/dev.129.16.3815

Chiang, C., Litingtung, Y., Lee, E., Young, K. E., Corden, J. L., Westphal, H. and Beachy, P. A. (1996). Cyclopia and defective axial patterning in mice lacking *Sonic hedgehog* gene function. *Nature* **383**, 407-413. doi:10.1038/383407a0

Cohen, M., Kicheva, A., Ribeiro, A., Blassberg, R., Page, K. M., Barnes, C. P. and Briscoe, J. (2015). Ptch1 and Gli regulate Shh signalling dynamics via multiple mechanisms. *Nat. Commun.* **6**, 6709. doi:10.1038/ncomms7709

Cook, O., Biehs, B. and Bier, E. (2004). *brinker* and *optomotor-blind* act coordinately to initiate development of the L5 wing vein primordium in *Drosophila*. *Development* **131**, 2113-2124. doi:10.1242/dev.01100

Corrigall, D., Walther, R. F., Rodriguez, L., Fichelson, P. and Pichaud, F. (2007). Hedgehog signaling is a principal inducer of Myosin-II-driven cell ingression in *Drosophila* epithelia. *Dev. Cell* **13**, 730-742. doi:10.1016/j.devcel.2007.09.015

Duda, M., Kirkland, N. J., Khalilgharibi, N., Tozluoglu, M., Yuen, A. C., Carpi, N., Bove, A., Piel, M., Charras, G., Baum, B. et al. (2019). Polarization of myosin II refines tissue material properties to buffer mechanical stress. *Dev. Cell* **48**, 245-260.e7. doi:10.1016/j.devcel.2018.12.020

Ellison, D., Mugler, A., Brennan, M. D., Lee, S. H., Huebner, R. J., Shamir, E. R., Woo, L. A., Kim, J., Amar, P., Nemenman, I. et al. (2016). Cell–cell communication enhances the capacity of cell ensembles to sense shallow gradients during morphogenesis. *Proc. Natl. Acad. Sci. USA* **113**, E679-E688. doi:10.1073/pnas.1516503113

Elowitz, M. B., Levine, A. J., Siggia, E. D. and Swain, P. S. (2002). Stochastic gene expression in a single cell. *Science* **297**, 1183-1186. doi:10.1126/science.1070919

Entchev, E. V. and Gonzàlez-Gaitàn, M. A. (2002). Morphogen gradient formation and vesicular trafficking. *Traffic* **3**, 98-109. doi:10.1034/j.1600-0854.2002.030203.x

Erdmann, T., Howard, M. and Ten Wolde, P. R. (2009). Role of spatial averaging in the precision of gene expression patterns. *Phys. Rev. Lett.* **103**, 258101. doi:10.1103/PhysRevLett.103.258101

Escudero, L. M., Costa, L. D. F., Kicheva, A., Briscoe, J., Freeman, M. and Babu, M. M. (2011). Epithelial organisation revealed by a network of cellular contacts. *Nat. Commun.* **2**, 526. doi:10.1038/ncomms1536

Etournay, R., Lepelletier, L., Boutet De Monvel, J., Michel, V., Cayet, N., Leibovici, M., Weil, D., Foucher, I., Hardelin, J. P. and Petit, C. (2010). Cochlear outer hair cells undergo an apical circumference remodeling constrained by the hair bundle shape. *Development* **137**, 1373-1383. doi:10.1242/dev.045138

Finegan, T. M., Na, D., Cammarota, C., Skeeters, A. V., Nadasi, T. J., Dawney, N. S., Fletcher, A. G., Oakes, P. W. and Bergstralh, D. T. (2019). Tissue tension and not interphase cell shape determines cell division orientation in the *Drosophila* follicular epithelium. *EMBO J.* **38**, e100072. doi:10.15252/embj.2018100072

Fried, P. and Iber, D. (2014). Dynamic scaling of morphogen gradients on growing domains. *Nat. Commun.* **5**, 5077. doi:10.1038/ncomms6077

Fried, P. and Iber, D. (2015). Read-out of dynamic morphogen gradients on growing domains. *PLoS One* **10**, e0143226. doi:10.1371/journal.pone.0143226

Gómez, H. F., Dumond, M. S., Hodel, L., Vetter, R. and Iber, D. (2021). 3D cell neighbour dynamics in growing pseudostratified epithelia. *Elife* **10**, e68135. doi:10.7554/eLife.68135

Gore, T., Matusek, T., D'Angelo, G., Giordano, C., Tognacci, T., Lavenant-Staccini, L., Rabouille, C. and Thérond, P. P. (2021). The GTPase Rab8 differentially controls the long- and short-range activity of the Hedgehog morphogen gradient by regulating Hedgehog apico-basal distribution. *Development* **148**, dev191791. doi:10.1242/dev.191791

Gregor, T., Mcgregor, A. P. and Wieschaus, E. F. (2008). Shape and function of the Bicoid morphogen gradient in dipteran species with different sized embryos. *Dev. Biol.* **316**, 350-358. doi:10.1016/j.ydbio.2008.01.039

Gregor, T., Tank, D. W., Wieschaus, E. F. and Bialek, W. (2007). Probing the limits to positional information. *Cell* **130**, 153-164. doi:10.1016/j.cell.2007.05.025

Gritli-Linde, A., Bei, M., Maas, R., Zhang, X. M., Linde, A. and Mcmahon, A. P. (2002). Shh signaling within the dental epithelium is necessary for cell proliferation, growth and polarization. *Development* **129**, 5323-5337. doi:10.1242/dev.00100

Guerrero, P., Perez-Carrasco, R., Zagorski, M., Page, D., Kicheva, A., Briscoe, J. and Page, K. M. (2019). Neuronal differentiation influences progenitor arrangement in the vertebrate neuroepithelium. *Development* **146**, dev176297. doi:10.1242/dev.176297

Hamaratoglu, F., De Lachapelle, A. M., Pyrowolakis, G., Bergmann, S. and Affolter, M. (2011). Dpp signaling activity requires pentagone to scale with tissue size in the growing *Drosophila* wing imaginal disc. *PLoS Biol.* **9**, e1001182. doi:10.1371/journal.pbio.1001182

Houchmandzadeh, B., Wieschaus, E. and Leibler, S. (2002). Establishment of developmental precision and proportions in the early *Drosophila* embryo. *Nature* **415**, 798-802. doi:10.1038/415798a

Hufnagel, L., Teleman, A. A., Rouault, H., Cohen, S. M. and Shraiman, B. I. (2007). On the mechanism of wing size determination in fly development. *Proc. Natl. Acad. Sci. USA* **104**, 3835-3840. doi:10.1073/pnas.0607134104

Iber, D. (2021). The control of lung branching morphogenesis. *Curr. Top. Dev. Biol.* **143**, 205-237.

Imuta, Y., Koyama, H., Shi, D., Eiraku, M., Fujimori, T. and Sasaki, H. (2014). Mechanical control of notochord morphogenesis by extra-embryonic tissues in mouse embryos. *Mech. Dev.* **132**, 44-58. doi:10.1016/j.mod.2014.01.004

Jaeger, J. and Verd, B. (2020). Dynamic positional information: patterning mechanism versus precision in gradient-driven systems. *Curr. Top. Dev. Biol.* **137**, 219-246. doi:10.1016/bs.ctdb.2019.11.017

Kadzik, R. S., Cohen, E. D., Morley, M. P., Stewart, K. M., Lu, M. M. and Morrisey, E. E. (2014). Wnt ligand/Frizzled 2 receptor signaling regulates tube shape and branch-point formation in the lung through control of epithelial cell shape. *Proc. Natl. Acad. Sci. USA* **111**, 12444-12449. doi:10.1073/pnas.1406639111

Kicheva, A., Pantazis, P., Bollenbach, T., Kalaidzidis, Y., Bittig, T., Jülicher, F. and González-Gaitán, M. (2007). Kinetics of morphogen gradient formation. *Science* **315**, 521-525. doi:10.1126/science.1135774

Kicheva, A., Bollenbach, T., Ribeiro, A., Valle, H. P., Lovell-Badge, R., Episkopou, V. and Briscoe, J. (2014). Coordination of progenitor specification and growth in mouse and chick spinal cord. *Science* **345**, 1254927. doi:10.1126/science.1254927

Kim, Y. K., Yu, H., Summers, V. R., Donaldson, K. J., Ferdous, S., Shelton, D., Zhang, N., Chrenek, M. A., Jiang, Y., Grossniklaus, H. E. et al. (2021). Morphometric analysis of retinal pigment epithelial cells from C57BL/6J mice during aging. *Invest. Ophth. Vis. Sci.* **62**, 32. doi:10.1167/iovs.62.2.32

Kokic, M., Iannini, A., Villa-Fombuena, G., Casares, F. and Iber, D. (2019). Minimisation of surface energy drives apical epithelial organisation and gives rise to Lewis' law. *BioRxiv* doi:10.1101/590729

Kondo, T. and Hayashi, S. (2015). Mechanisms of cell height changes that mediate epithelial invagination. *Dev. Growth Differ.* **57**, 313-323. doi:10.1111/dgd.12224

Ku, H.-Y. and Sun, Y. H. (2017). Notch-dependent epithelial fold determines boundary formation between developmental fields in the *Drosophila* antenna. *PLoS Genet.* **13**, e1006898. doi:10.1371/journal.pgen.1006898

Lander, A. D., Nie, Q. and Wan, F. Y. M. (2002). Do Morphogen gradients arise by diffusion? *Dev. Cell* **2**, 785-796. doi:10.1016/s1534-5807(02)00179-x

Lander, A. D., Lo, W.-C., Nie, Q. and Wan, F. Y. M. (2009). The measure of success: constraints, objectives, and tradeoffs in Morphogen-mediated patterning. *CSH Perspect. Biol.* **1**, a002022. doi:10.1101/cshperspect.a002022

Legoff, L., Rouault, H. and Lecuit, T. (2013). A global pattern of mechanical stress polarizes cell divisions and cell shape in the growing *Drosophila* wing disc. *Development* **140**, 4051-4059. doi:10.1242/dev.090878

Long, Y., Vetter, R. and Iber, D. (2023). 2d effects enhance precision of gradient-based tissue patterning. *BioRxiv.* doi:10.1101/2023.03.13.532369

Mateus, R., Holtzer, L., Seum, C., Hadjivasiliou, Z., Dubois, M., Jülicher, F. and Gonzalez-Gaitan, M. (2020). BMP signaling gradient scaling in the zebrafish pectoral fin. *Cell. Rep.* **30**, 4292-4302.e7. doi:10.1016/j.celrep.2020.03.024

Matsuda, S., Schaefer, J. V., Mii, Y., Hori, Y., Bieli, D., Taira, M., Plückthun, A. and Affolter, M. (2021). Asymmetric requirement of Dpp/BMP morphogen dispersal in the *Drosophila* wing disc. *Nat. Commun.* **12**, 6435. doi:10.1038/s41467-021-26726-6

Morishita, Y. and Iwasa, Y. (2009). Accuracy of positional information provided by multiple morphogen gradients with correlated noise. *Phys. Rev. E* **79**, 061905. doi:10.1103/PhysRevE.79.061905

Morishita, Y. and Iwasa, Y. (2011). Coding design of positional information for robust morphogenesis. *Biophys. J.* **101**, 2324-2335. doi:10.1016/j.bpj.2011.09.048

Mugler, A., Levchenko, A. and Nemenman, I. (2016). Limits to the precision of gradient sensing with spatial communication and temporal integration. *Proc. Natl. Acad. Sci. USA* **113**, E689-E695. doi:10.1073/pnas.1509597112

Neufeld, T. P., De La Cruz, A. F. A., Johnston, L. A. and Edgar, B. A. (1998). Coordination of growth and cell division in the *Drosophila* wing. *Cell* **93**, 1183-1193. doi:10.1016/S0092-8674(00)81462-2

Osterfield, M., Berg, C. A. and Shvartsman, S. Y. (2017). Epithelial patterning, morphogenesis, and evolution: *Drosophila* eggshell as a model. *Dev. Cell* **41**, 337-348. doi:10.1016/j.devcel.2017.02.018

Pera, E., Stein, S. and Kessel, M. (1999). Ectodermal patterning in the avian embryo: epidermis versus neural plate. *Development* **126**, 63-73. doi:10.1242/dev.126.1.63

Raser, J. M. and O'Shea, E. K. (2005). Noise in gene expression: origins, consequences, and control. *Science* **309**, 2010-2013. doi:10.1126/science.1105891

Restrepo, S., Zartman, J. J. and Basler, K. (2014). Coordination of patterning and growth by the morphogen dpp. *Curr. Biol.* **24**, R245-R255. doi:10.1016/j.cub.2014.01.055

Reyes, R., Lander, A. and Nahmad, M. (2022). Dynamic readout of the Hh gradient in the drosophila wing disc reveals pattern-specific tradeoffs between robustness and precision. *BioRxiv*. doi:10.1101/2022.12.21.521489

Rupprecht, J. F., Ong, K. H., Yin, J., Huang, A., Dinh, H. H., Singh, A. P., Zhang, S., Yu, W. and Saunders, T. E. (2017). Geometric constraints alter cell arrangements within curved epithelial tissues. *Mol. Biol. Cell* **28**, 3582-3594. doi:10.1091/mbc.e17-01-0060

Saade, M., Gutierrez-Vallejo, I., Le Dreau, G., Rabadan, M. A., Miguez, D. G., Buceta, J. and Marti, E. (2013). Sonic Hedgehog signaling switches the mode of division in the developing nervous system. *Cell Rep.* **4**, 492-503. doi:10.1016/j.celrep.2013.06.038

Saitoh, M., Shirakihara, T., Fukasawa, A., Horiguchi, K., Sakamoto, K., Sugiya, H., Beppu, H., Fujita, Y., Morita, I., Miyazono, K. et al. (2013). Basolateral BMP signaling in polarized epithelial cells. *PLoS One* **8**, e62659. doi:10.1371/journal.pone.0062659

Sánchez-Gutiérrez, D., Tozluoglu, M., Barry, J. D., Pascual, A., Mao, Y. and Escudero, L. M. (2016). Fundamental physical cellular constraints drive self-organization of tissues. *EMBO J.* **35**, 77-88. doi:10.15252/embj.201592374

Skouloudaki, K., Papadopoulos, D. K., Tomancak, P. and Knust, E. (2019). The apical protein Apnoia interacts with Crumbs to regulate tracheal growth and inflation. *PLoS Genet.* **15**, e1007852. doi:10.1371/journal.pgen.1007852

Sokolowski, T. R. and Tkačik, G. (2015). Optimizing information flow in small genetic networks. iv. spatial coupling. *Phys. Rev. E* **91**, 062710. doi:10.1103/PhysRevE.91.062710

Sturtevant, M. A., Biehs, B., Marin, E. and Bier, E. (1997). The spalt gene links the A/P compartment boundary to a linear adult structure in the *Drosophila* wing. *Development* **124**, 21-32. doi:10.1242/dev.124.1.21

Tkačik, G., Dubuis, J. O., Petkova, M. D. and Gregor, T. (2015). Positional information, positional error, and readout precision in morphogenesis: a mathematical framework. *Genetics* **199**, 39-59. doi:10.1534/genetics.114.171850

Tomoyasu, Y., Ueno, N. and Nakamura, M. (2000). The Decapentaplegic morphogen gradient regulates the notal *wingless* expression through induction of *pannier* and *u-shaped* in *Drosophila*. *Mech. Dev.* **96**, 37-49. doi:10.1016/S0925-4773(00)00374-9

Tripathi, B. K. and Irvine, K. D. (2022). The wing imaginal disc. *Genetics* **220**, iyac020. doi:10.1093/genetics/iyac020

Tsai, T. Y.-C., Sikora, M., Xia, P., Colak-Champollion, T., Knaut, H., Heisenberg, C.-P. and Megason, S. G. (2020). An adhesion code ensures robust pattern formation during tissue morphogenesis. *Science* **370**, 113-116. doi:10.1126/science.aba6637

Urban, E. A. and Johnston, R. J. (2018). Buffering and amplifying transcriptional noise during cell fate specification. *Front. Genet.* **9**, 591. doi:10.3389/fgene.2018.00591

Vetter, R. and Iber, D. (2022). Precision of morphogen gradients in neural tube development. *Nat. Commun.* **13**, 1145. doi:10.1038/s41467-022-28834-3

Wartlick, O., Mumcu, P., Kicheva, A., Bittig, T., Seum, C., Jülicher, F. and González-Gaitán, M. (2011). Dynamics of Dpp signaling and proliferation control. *Science* **331**, 1154-1159. doi:10.1126/science.1200037

Wartlick, O., Jülicher, F. and Gonzalez-Gaitan, M. (2014). Growth control by a moving morphogen gradient during *Drosophila* eye development. *Development* **141**, 1884-1893. doi:10.1242/dev.105650

Widmann, T. J. and Dahmann, C. (2009). Dpp signaling promotes the cuboidal-to-columnar shape transition of *Drosophila* wing disc epithelia by regulating Rho1. *J. Cell Sci.* **122**, 1362-1373. doi:10.1242/jcs.044271

Wolpert, L. (1969). Positional information and the spatial pattern of cellular differentiation. *J. Theor. Biol.* **25**, 1-47. doi:10.1016/S0022-5193(69)80016-0

Xiong, F., Tentner, A. R., Huang, P., Gelas, A., Mosaliganti, K. R., Souhait, L., Rannou, N., Swinburne, I. A., Obholzer, N. D., Cowgill, P. D. et al. (2013). Specified neural progenitors sort to form sharp domains after noisy shh signaling. *Cell* **153**, 550-561. doi:10.1016/j.cell.2013.03.023

Yokouchi, M., Atsugi, T., Van Logtestijn, M., Tanaka, R. J., Kajimura, M., Suematsu, M., Furuse, M., Amagai, M. and Kubo, A. (2016). Epidermal cell turnover across tight junctions based on Kelvin's tetrakaidecahedron cell shape. *Elife* **5**, e19593. doi:10.7554/eLife.19593

Yu, S. R., Burkhardt, M., Nowak, M., Ries, J., Petrasek, Z., Scholpp, S., Schwille, P. and Brand, M. (2009). Fgf8 morphogen gradient forms by a source-sink mechanism with freely diffusing molecules. *Nature* **461**, 533-536. doi:10.1038/nature08391

Zagorski, M., Tabata, Y., Brandenberg, N., Lutolf, M. P., Tkacik, G., Bollenbach, T., Briscoe, J. and Kicheva, A. (2017). Decoding of position in the developing neural tube from antiparallel morphogen gradients. *Science* **356**, 1379-1383. doi:10.1126/science.aam5887

Zhang, Z., Zwick, S., Loew, E., Grimley, J. S. and Ramanathan, S. (2019). Mouse embryo geometry drives formation of robust signaling gradients through receptor localization. *Nat. Commun.* **10**, 4516. doi:10.1038/s41467-019-12533-7

Zoller, B., Nicolas, D., Molina, N. and Naef, F. (2015). Structure of silent transcription intervals and noise characteristics of mammalian genes. *Mol. Syst. Biol.* **11**, 823. doi:10.15252/msb.20156257

In this supplementary document, we theoretically show that averaging morphogen concentrations over a spatial region (such as cell areas) can shift the effective readout position compared to point-like readout, and we derive the corresponding shift Δx analytically for isotropic and for rectangular cell shapes. We focus on exponential morphogen gradients here as they arise in systems with diffusion-driven morphogen transport and uniform linear degradation, but note that the developed formalism can be applied directly also to other gradient shapes. Moreover, the impact of spatial correlation of the kinetic cell parameters on the positional error, the choice of the kinetic parameter distribution and the effect of cell number in the source domain are discussed.

Readout in a continuous domain

Consider an exponential morphogen concentration gradient

$$C(x) = C_0 \exp\left[-\frac{x}{\lambda}\right]$$

with concentration C_0 at the source at $x = 0$, and decay length λ. Assuming a continuous readout based on a threshold concentration $C_\theta = C(x_\theta)$, a positional identity boundary forms at position

$$x_\theta = \lambda \ln\left[\frac{C_0}{C_\theta}\right]. \tag{S1}$$

This mechanism allows for gradient-based tissue patterning, where individual patterning domains are delineated by different boundary positions x_θ resulting from different readout thresholds C_θ.

Readout in a tissue of isotropic cells

For morphogen readout in a cellular tissue, we consider several different cases in a unified description. Cells can either sense the morphogen concentration at a singular point, averaged over a spatial region with radius r about that point (which may or may not be smaller than a cell), or as an average concentration over the entire cell area. We denote this readout region by Ω (Fig. S1). The average concentration in Ω is

$$\langle C \rangle = \frac{\int_\Omega C(x)\, d\Omega}{\int_\Omega d\Omega}.$$

Assuming that the averaging domain is circular (i.e., the cell areas have no orientational bias) in a two-dimensional tissue cross section or surface, we can approximate Ω as a disk with radius r about a center point $(x_0, 0)$:

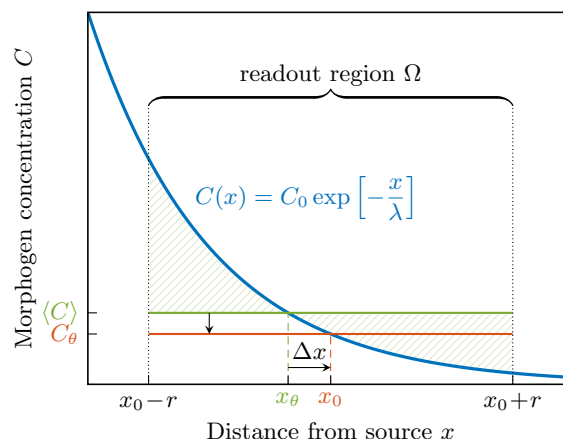$$\Omega = \left\{ (x, y) \mid (x - x_0)^2 + y^2 < r^2 \right\}.$$

Fig. S1. Averaging an exponential morphogen concentration (blue) over a local region such as the cell area leads to a larger readout concentration (green) than taking the concentration at the middle of the region (red). To compensate for this effect, the readout position shifts downhill (away from the source) by a distance Δx from x_θ to x_0.

In the case where the concentration is averaged over the entire cell area, r is the effective cell radius. The average concentration thus becomes

$$\langle C \rangle = \frac{C_0}{\pi r^2} \int_\Omega \exp\left[-\frac{x}{\lambda}\right] d\Omega$$
$$= \frac{C_0}{\pi r^2} 2\pi r \lambda \exp\left[-\frac{x_0}{\lambda}\right] I_1\left(\frac{r}{\lambda}\right)$$

where

$$I_n(z) = \sum_{k=0}^{\infty} \frac{(z/2)^{2k+n}}{k!(k+n)!}$$

is the modified Bessel function of the first kind for integer n. The series converges very quickly if $r \ll \lambda$, such that higher order terms in r/λ can be dropped. Substitution and expansion of the Bessel function yields

$$\langle C \rangle = C(x_0) \frac{2\lambda}{r} I_1\left(\frac{r}{\lambda}\right)$$
$$= C(x_0) \sum_{k=0}^{\infty} \frac{(r/2\lambda)^{2k}}{k!(k+1)!}$$
$$= C(x_0)\left[1 + \frac{1}{8}\left(\frac{r}{\lambda}\right)^2 + \frac{1}{192}\left(\frac{r}{\lambda}\right)^4 + \mathcal{O}\left(\left(\frac{r}{\lambda}\right)^6\right)\right].$$

Thus, the mean concentration $\langle C \rangle$ is larger than the one in the middle of the readout domain, $C(x_0)$, and this deviation increases with larger readout regions and shorter gradient decay lengths.
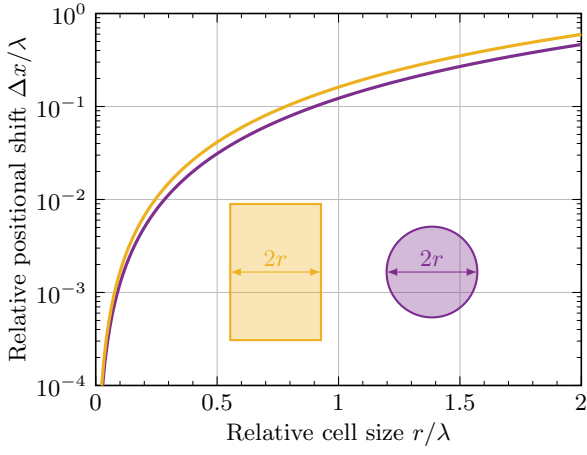
Fig. S2. Readout boundary shift due to spatial averaging as a function of the size over which the morphogen concentration is averaged. The purple line shows the isotropic case with a circular averaging region (Eq. S2); the orange line represents the case with rectangular cells (Eq. S4).

If threshold-based readout operates on the averaged concentration, we must have $C_\theta = \langle C \rangle$. Therefore,

$$\frac{C(x_\theta)}{C(x_0)} = \exp\left[-\frac{x_\theta - x_0}{\lambda}\right] = \sum_{k=0}^{\infty} \frac{(r/2\lambda)^{2k}}{k!(k+1)!}.$$

The location of domain boundaries is shifted down the concentration gradient by the distance

$$\Delta x = x_0 - x_\theta = \lambda \ln\left[\sum_{k=0}^{\infty} \frac{(r/2\lambda)^{2k}}{k!(k+1)!}\right] \qquad (S2)$$

as shown in Fig. S1. Notably, the shift is independent of both the gradient amplitude C_0 and the concentration threshold C_θ for an exponential gradient. Therefore, it is the same for all readout positions in the pattern if the averaging radius r and the decay length λ are spatially invariant, such that all domain boundaries are shifted equally by this averaging effect. Eq. S2 is plotted in Fig. S2.

Using the power series expansion of the natural logarithm,

$$\ln[1 + x] = \sum_{k=1}^{\infty} (-1)^{k+1} \frac{x^k}{k} = x - \frac{x^2}{2} + \mathcal{O}\left(x^3\right),$$

the boundary shift can be expanded to

$$\Delta x = \lambda \left[\frac{1}{8}\left(\frac{r}{\lambda}\right)^2 - \frac{1}{384}\left(\frac{r}{\lambda}\right)^4 + \mathcal{O}\left(\left(\frac{r}{\lambda}\right)^6\right)\right].$$

For a mean cell radius of $r = 2.5\,\mu\text{m}$ and a gradient decay length of $\lambda = 20\,\mu\text{m}$, the shift is $\Delta x \approx 0.039\,\mu\text{m}$.

By combining Eqs. S1 and S2, we find the mean domain boundary position at

$$x_0 = x_\theta + \Delta x = \lambda \ln\left[\frac{C_0}{C_\theta} \sum_{k=0}^{\infty} \frac{(r/2\lambda)^{2k}}{k!(k+1)!}\right]. \qquad (S3)$$

Readout in a tissue of rectangular cells

We now derive the downhill shift Δx also for rectangular cell areas, effectively rendering the problem one-dimensional. This scenario corresponds to a tissue composed of cuboidal cells in which the morphogen gradient forms in a direction perpendicular to one of the cells' axes. In this case,

$$\Omega = \{(x,y) \mid |x - x_0| < r\}.$$

Averaging over the cell area thus gives

$$\langle C \rangle = \frac{C_0}{2r} \int_\Omega \exp\left[-\frac{x}{\lambda}\right] d\Omega$$
$$= C(x_0) \frac{\lambda}{r} \sinh\left[\frac{r}{\lambda}\right]$$

Requiring again that the readout threshold be the average concentration, $C_\theta = \langle C \rangle$, yields

$$\frac{C(x_\theta)}{C(x_0)} = \exp\left[-\frac{x_\theta - x_0}{\lambda}\right] = \frac{\lambda}{r} \sinh\left[\frac{r}{\lambda}\right].$$

The shift in the readout position then follows as

$$\Delta x = x_0 - x_\theta = \lambda \ln\left[\frac{\lambda}{r} \sinh\left(\frac{r}{\lambda}\right)\right] \qquad (S4)$$

which expands to

$$\Delta x = \lambda \left[\frac{1}{6}\left(\frac{r}{\lambda}\right)^2 - \frac{1}{180}\left(\frac{r}{\lambda}\right)^4 + \mathcal{O}\left(\left(\frac{r}{\lambda}\right)^6\right)\right].$$

Eq. S4 is plotted in Fig. S2. For a mean cell radius of $r = 2.5\,\mu\text{m}$ (which in this case corresponds to the half-width of the rectangular cells) and a gradient decay length of $\lambda = 20\,\mu\text{m}$, the shift is $\Delta x \approx 0.052\,\mu\text{m}$.

In analogy to Eq. S3, the mean domain boundary position is found at

$$x_0 = x_\theta + \Delta x = \lambda \ln\left[\frac{C_0}{C_\theta}\frac{\lambda}{r} \sinh\left(\frac{r}{\lambda}\right)\right].$$

in tissues composed of rectangular cells.

Impact of spatial correlation on the positional error

In the main article, we assumed uncorrelated morphogen kinetics. Here, we demonstrate how spatial correlation affects the positional error. First, we consider total correlation, where all three kinetic parameters (p, d, D) are the same for all cells, but are still varied between different simulations (different tissues). In this limiting case, morphogen gradient variability occurs only between tissues, not within them. The positional error is significantly greater than with independent cells, and the square-root scaling is lost (Fig. S3, green triangles), because to the morphogen gradient, the tissue effectively appears like a homogeneous continuum with uniform properties.

Next, we consider, as a second extreme case, a maximal degree of cell-to-cell correlation in the kinetic parameters, while preserving their probability distributions within the tissue. The kinetic cell parameters (p_i, d_i, D_i) are drawn individually and independently for each cell, but are then sorted along the patterning axis and assigned to the cells i, prior to solving the reaction-diffusion equation. Sorting does not affect the patterning precision appreciably, independent of the ordering (Fig. S3). In comparison to zero correlation, sorting slightly reduces the positional error—an effect that is most pronounced for larger cell diameters. But even with this maximal level of spatial cell-to-cell correlation, the square-root scaling of the positional error holds. Intermediate levels of spatial correlation can be expected to yield positional errors lying in between the curves for zero and maximal cell-to-cell correlation.
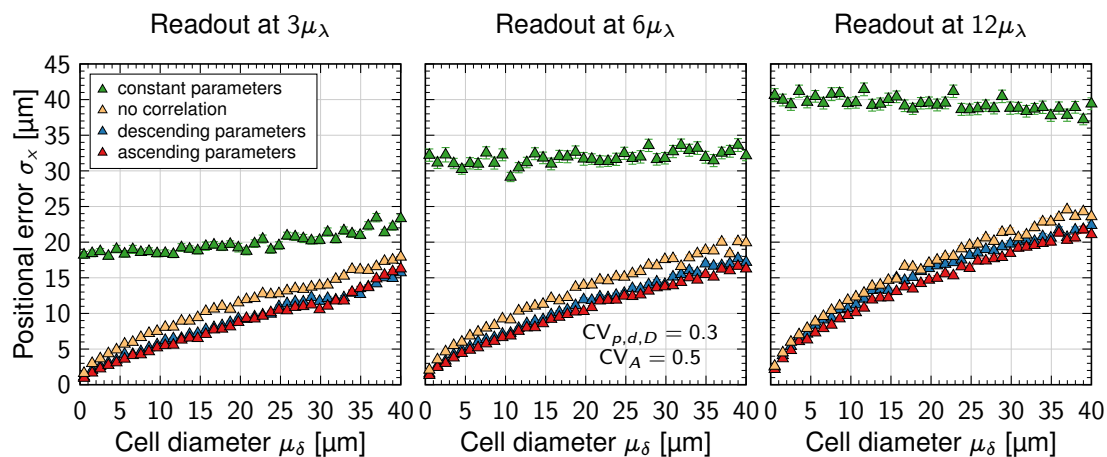
Fig. S3. **Impact of correlation on the positional error at different readout positions and cell diameters.** Green triangles represent total correlation (all cells have equal kinetic parameters), yellow triangles represent no correlation (as presented in the main Fig. 4F). Blue (red) triangles correspond to the case with maximal spatial correlation at given cell-to-cell variability $\mathrm{CV}_{p,d,D}$, where the cell parameters were drawn from log-normal distributions and then sorted in descending (ascending) order. All simulations were repeated $n = 10^3$ times and the mean positional error $\pm$ SEM is plotted.

Choice of the kinetic parameter distribution

In the main article, we assumed log-normally distributed morphogen kinetics. In this section, we show that our results are largely independent of the probability distribution assumed for the kinetic parameters, provided that it meets certain physiological criteria:

- The morphogen production rates, degradation rates and diffusivities must be strictly positive. This rules out a normal distribution.

- The probability density of near-zero kinetic parameters must vanish quickly, as otherwise no successful patterning can occur. For example, a tiny diffusion coefficient would not enable morphogen transport over biologically useful distances within useful time periods. This rules out a normal distribution truncated at zero, because very low diffusivities would occur rather frequently for such a distribution.

We repeated the simulations shown in Figs. 2A,B and 4F with a gamma distribution in place of the log-normal distribution. Among other distributions that are conceivable, a gamma distribution with appropriate shape parameter α and inverse scale parameter β fulfills the above criteria. In order to recover the mean and variance of the kinetic parameters, we set $\alpha_k = 1/\mathrm{CV}_k^2$ and $\beta_k = \mathrm{CV}_k^2/\mu_k$, where CV_k is the coefficient of variation and μ_k the mean value of a specific kinetic parameter k. As can be appreciated from Fig. S4, the results are not significantly altered by the specific choice of probability distribution, and our conclusions remain valid. The scaling exponents are consistent within statistical errors.

Effect of cell number in the source domain on gradient precision

In the main article, we showed that patterning precision increases with narrower cells and wider sources. These effects are coupled—wider sources will be composed of more cells if the average cell diameter remains constant. In this section, we demonstrate that the positional error is mainly dominated by the cell diameter rather than the source size, and that the found scaling $\sigma_x \sim 1/L_s$ (Eq. 6) is largely due to higher cell numbers in wider sources.

Increasing the number of cells in a source of fixed length improves the precision of the morphogen gradient parameters
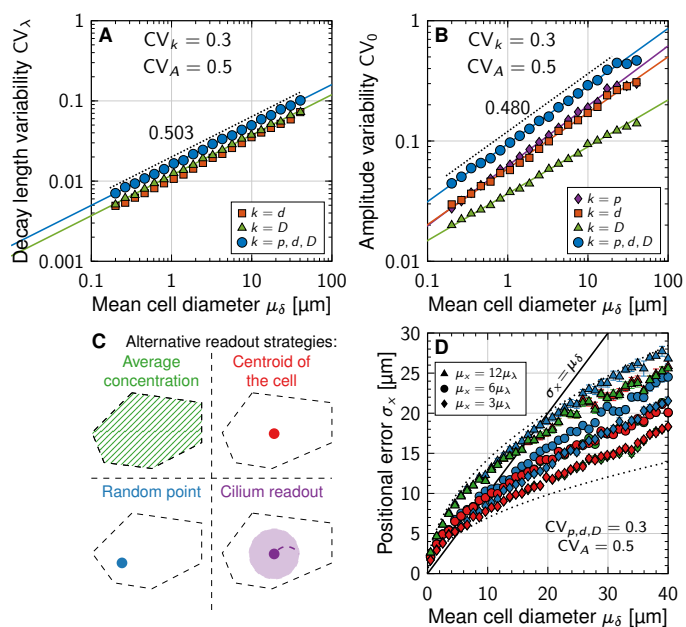

Fig. S4. Gradient variability and positional error under gamma-distributed morphogen kinetics. All simulations were repeated $n = 10^3$ times and the mean values $\pm$ SEM are plotted. **A,B** The same scaling laws for the gradient variability found for the gamma and log-normal distributions (Fig. 2A,B) are consistent. **C** Different readout strategies (identical to Fig. 4A). **D** Square-root scaling of the positional error with the cell diameter is found also with gamma-distributed morphogen kinetics. Symbol colours in D correspond to the different morphogen sensing strategies in C.

according to the asymptotic relationship

$$\mathrm{CV}_{\lambda,0} \sim \sqrt{\frac{\mu_{\delta_s}}{L_s}} \sim \sqrt{\frac{1}{N_\mathrm{cells}}},$$

where N_cells is the number of cells in the source domain (Fig. S5A,B). They thus approximately follow the law of large numbers. The positional error decreases analogously with increased cell number in a source of fixed length (Fig. S5C). If, on the other hand, the number of source cells is fixed but the
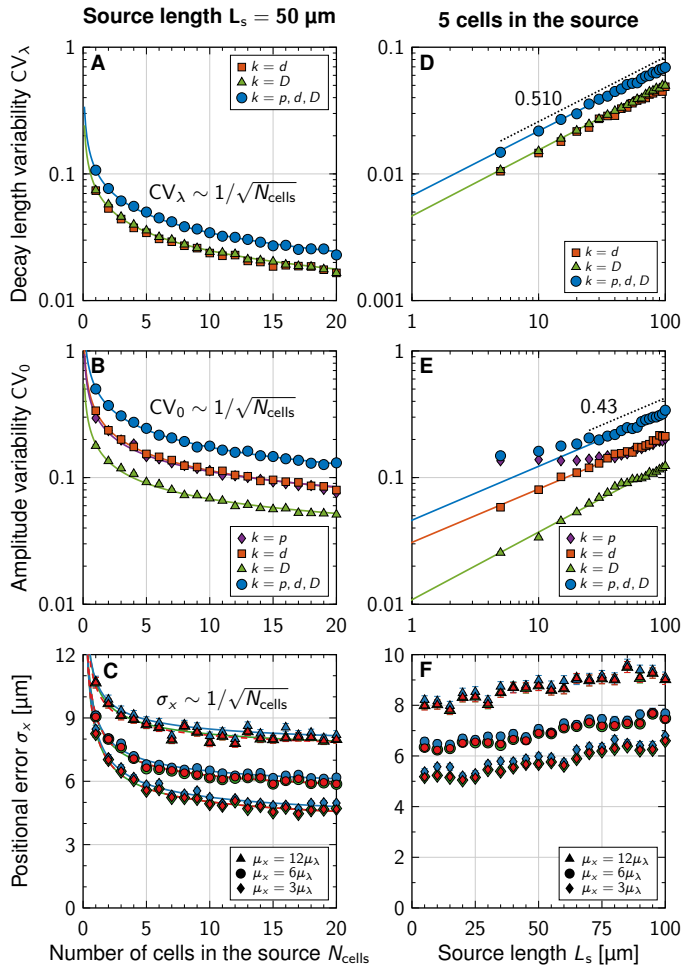
Source length $L_s = 50$ µm (columns A, B, C) and **5 cells in the source** (columns D, E, F)

source size increases, the variability in the gradient parameters increases according to power laws (Fig. S5D,E),

$$\mathrm{CV}_{\lambda,0} \sim \mu_\delta^\alpha \quad \text{and} \quad \mathrm{CV}_0 \sim \mu_\delta^\beta \qquad (S5)$$

with exponents $\alpha = 0.510 \pm 0.005$ (Fig. S5D, blue curve) and $\beta = 0.43 \pm 0.02$ (Fig. S5E, blue curve), suggesting again $\mathrm{CV}_{\lambda,0} \sim \sqrt{\mu_{\delta_s}/L_s}$. A source composed of a fixed number of cells yields only a mildly greater positional error if its constituent cells have a larger average diameter, however (Fig. S5F). In these simulations, the mean cell diameter in the patterning domain was fixed. Thus, in order to achieve high spatial gradient precision, a morphogen source must have a large number of cells with small diameters, but the cell count is more decisive than the source length.

To study the competition of cell sizes between the source and patterning domain, we then changed the mean cell diameter separately in both subdomains, retaining the mean diameter in the other at a constant value. No further appreciable increase in gradient precision takes place once the mean cell diameter in the source subceeds the one in the patterning domain ($\mu_{\delta_s} < \mu_{\delta_p}$, Fig. S6). The mean cell diameter in the source has a limited impact on gradient precision (Fig. S6, pink symbols) compared to the mean diameter in the patterning domain (Fig. S6, yellow symbols). Overall, this suggests that a large number of narrow cells in both the source and patterning domain, but mainly in the latter, is advantageous for patterning precision.

Fit parameters

In Table S1, we list all functional relationships used to fit the data shown in the main article and this supplementary document, together with the fit parameters and their standard errors (SE).

Figure S5: Effect of source length and number of source cells on gradients precision. A,B In a source of fixed length L_s, there is less variability in the gradient parameters λ and C_0 as the number of constituting cells increases. **C** The positional error decreases with more cells in a source of fixed length, but saturates beyond about 5 source cells. **D,E** The gradient parameters become more variable in wider sources consisting of a fixed number of cells. **F** The positional error mildly increases in wider morphogen sources with fixed cell count. Colours in C,F correspond to readout strategies shown in Fig. S4C. All data points show mean values $\pm$ SEM from $n = 10^3$ simulations. Model parameters: $\mu_{\delta_p} = 5$ µm, $\mathrm{CV}_{p,d,D} = 0.3$, $\mathrm{CV}_A = 0.5$, $\mu_\lambda = 20$ µm.

Fig. S6. Separate effects of the mean cell diameter in the source and patterning domains on the positional error. A,B,C Change of positional error at $\mu_x = 3\mu_\lambda = 60$ µm, as the mean cell diameter is varied only in the source ($\mu_\delta = \mu_{\delta_s}$, pink), only in the pattern ($\mu_\delta = \mu_{\delta_p}$, yellow) or in both simultaneously ($\mu_\delta = \mu_{\delta_s} = \mu_{\delta_p}$, blue), but is fixed elsewhere (at 2, 5, 10 µm in A, B, C, respectively). All simulations were repeated $n = 10^3$ times and the mean values $\pm$ SEM are plotted. Model parameters: $L_s = 5\mu_{\delta_s}$, $\mathrm{CV}_{p,d,D} = 0.3$, $\mathrm{CV}_A = 0.5$.

Table S1. Summary of the fit functions and their parameters. All lengths are in micrometres.

Figure	Model	Legend entry	a	SE(a)	b	SE(b)
2A	$\ln \mathrm{CV}_\lambda = a \ln \mu_\delta + b$	$k = D$	0.507	0.002	−4.528	0.004
		$k = p, d, D$	0.510	0.004	−4.199	0.008
2B	$\ln \mathrm{CV}_0 = a \ln \mu_\delta + b$	$k = p$	0.497	0.003	−4.528	0.004
		$k = d$	0.457	0.004	−2.847	0.006
		$k = D$	0.387	0.006	−3.403	0.008
		$k = p, d, D$	0.472	0.005	−2.396	0.007
2E	$\mathrm{CV}_\lambda = b$	$k = D$	—	—	0.0249	0.0001
		$k = p, d, D$	—	—	0.0343	0.0001
2F	$\mathrm{CV}_0 = a/L_\mathrm{s} + b$	$k = p$	1.087	0.038	0.095	0.002
		$k = D$	−0.158	0.010	0.070	0.001
		$k = p, d, D$	0.870	0.025	0.160	0.001
2G	$\mathrm{CV}_\lambda = b$	$k = d$	—	—	0.0238	0.0002
		$k = D$	—	—	0.0246	0.0001
		$k = p, d, D$	—	—	0.0338	0.0001
4D	$\sigma_x = a\mu_\lambda + b$	$\mu_x = 3\mu_\lambda$ average	0.097	0.004	3.4	0.1
		$\mu_x = 3\mu_\lambda$ centroid	0.087	0.004	3.4	0.1
		$\mu_x = 3\mu_\lambda$ random	0.096	0.004	3.7	0.1
		$\mu_x = 6\mu_\lambda$ average	0.083	0.003	4.9	0.1
		$\mu_x = 6\mu_\lambda$ centroid	0.083	0.003	4.9	0.1
		$\mu_x = 6\mu_\lambda$ random	0.083	0.003	5.1	0.1
4D	$\sigma_x = a\mu_\lambda^2 + b$	$\mu_x = 12\mu_\lambda$ average	0.0014	0.0001	7.8	0.1
		$\mu_x = 12\mu_\lambda$ centroid	0.0014	0.0001	7.8	0.1
		$\mu_x = 12\mu_\lambda$ random	0.0014	0.0001	7.9	0.1
4E	$\sigma_x = a/L_\mathrm{s} + b$	$\mu_x = 3\mu_\lambda$ average	12.5	0.9	4.75	0.05
		$\mu_x = 3\mu_\lambda$ centroid	12.6	0.8	4.74	0.05
		$\mu_x = 3\mu_\lambda$ random	12.3	1.0	5.01	0.05
		$\mu_x = 6\mu_\lambda$ average	11.4	0.6	6.01	0.03
		$\mu_x = 6\mu_\lambda$ centroid	11.3	0.6	6.01	0.03
		$\mu_x = 6\mu_\lambda$ random	10.9	0.6	6.20	0.03
		$\mu_x = 12\mu_\lambda$ average	8.9	1.0	8.01	0.06
		$\mu_x = 12\mu_\lambda$ centroid	8.9	1.0	8.01	0.06
		$\mu_x = 12\mu_\lambda$ random	8.5	1.0	8.24	0.05
4G	$\sigma_x = a\sqrt{\mu_x} + b$	average	0.429	0.003	1.86	0.06
		centroid	0.429	0.003	1.85	0.06
		random	0.421	0.003	2.17	0.07
5D	$\mathrm{CV}_x = a/\sqrt{L_\mathrm{p}} + b$		1.28	0.02	−0.039	0.002
S5A	$\mathrm{CV}_\lambda = a/\sqrt{N_\mathrm{cells}}$	$k = D$	0.0778	0.0006	—	—
		$k = p, d, D$	0.1082	0.0005	—	—
S5B	$\mathrm{CV}_0 = a/\sqrt{N_\mathrm{cells}} + b$	$k = p$	0.293	0.009	0.019	0.004
		$k = d$	0.325	0.003	0.011	0.001
		$k = D$	0.171	0.004	0.014	0.002
		$k = p, d, D$	0.490	0.006	0.019	0.003
S5C	$\sigma_x = a/N_\mathrm{cells} + b$	$\mu_x = 3\mu_\lambda$ average	4.9	0.2	3.48	0.06
		$\mu_x = 3\mu_\lambda$ centroid	4.9	0.2	3.47	0.06
		$\mu_x = 3\mu_\lambda$ random	4.8	0.2	3.73	0.07
		$\mu_x = 6\mu_\lambda$ average	4.2	0.1	4.94	0.06
		$\mu_x = 6\mu_\lambda$ centroid	4.2	0.1	4.95	0.05
		$\mu_x = 6\mu_\lambda$ random	3.9	0.1	5.25	0.05
		$\mu_x = 12\mu_\lambda$ average	3.6	0.2	7.10	0.10
		$\mu_x = 12\mu_\lambda$ centroid	3.6	0.2	7.10	0.10
		$\mu_x = 12\mu_\lambda$ random	3.4	0.2	7.40	0.10
S5D	$\ln \mathrm{CV}_\lambda = a \ln L_\mathrm{s} + b$	$k = D$	0.520	0.004	−5.38	0.01
		$k = p, d, D$	0.510	0.006	−5.01	0.02
S5E	$\ln \mathrm{CV}_0 = a \ln L_\mathrm{s} + b$	$k = d$	0.42	0.01	−3.48	0.03
		$k = D$	0.53	0.01	−4.52	0.05
		$k = p, d, D$	0.43	0.02	−3.08	0.07